Multiscale Light Field Microscopy Platform for Multi-purpose Dynamic Volumetric Bioimaging

Yangyang Bai[1,2], Matt Jones[1], Lauro Sebastian Ojeda[1,2], Janielle Cuala[4], Lynne Cherchia[1,2], Senta K. Georgia[5,6], Scott E. Fraser[1,2,3], Thai V. Truong[1,3*]

[1] Translational Imaging Center, University of Southern California; Los Angeles, CA, USA.

[2] Biomedical Engineering, University of Southern California; Los Angeles, CA, USA.

[3] Molecular and Computational Biology, University of Southern California; Los Angeles, CA, USA.

[4] Medical Biophysics Program, Keck School of Medicine, University of Southern California, Los Angeles, CA.

[5] Department of Pediatrics, Keck School of Medicine, University of Southern California, Los Angeles, CA.

[6] Center for Endocrinology, Diabetes, and Metabolism, The Saban Research Institute, Children's Hospital Los Angeles, Los Angeles, CA

* Corresponding author. Email: tvtruong@usc.edu

Light field microscopy (LFM) has emerged in recent years as a unique solution for fast, scan-free volumetric imaging of dynamic biological samples. This is achieved by using a microlens array in the detection path to record both the lateral and angular information of the light fields coming from the sample, capturing a 3-dimensional (3D) volume in a single 2-dimensional (2D) snapshot. In post-acquisition, the 3D sample volume is computationally reconstructed from the recorded 2D images, thus enabling unprecedented 3D capture speed, not limited by the typical constraint of physically scanning the focal plane over the sample volume. Up to date, most published LFM imaging setups have been specialized single-purpose platforms, optimized for a narrow performance window in field of view and resolution, thus hampering widespread adoption of LFM for biomedical research. Here, we present a versatile LFM platform for fast 3D imaging across multiple scales, enabling applications from cell to system-level biology on the same imaging setup. Our multiscale LFM is built as an add-on module to a conventional commercially available wide field microscope, and the various imaging applications, with different ranges of field of view and resolution, are achieved by simply switching between the standard microscope objectives available on the wide field microscope. Additionally, we provide an open-source end-to-end software package for calculating the system performance parameters, processing the experimentally measured point spread function, and light field 3D image reconstruction. We demonstrate the performance of our multiscale LFM platform through imaging the whole-brain activity map of seizures in larval zebrafish, calcium dynamics in ex vivo mouse pancreatic islets, and subcellular protein dynamics in cultured cells.

I. INTRODUCTION

Biological processes inherently occur in three dimensions (3D), ranging from intra-cellular trafficking to whole brain neural network activity[1–3]. Observing these processes in their native 3D context is essential for gaining a comprehensive understanding of how living systems develop, and how they function in health and malfunction in disease[4–6]. Volumetric microscopy techniques have greatly advanced our understanding of dynamic biological systems in 3D, yet challenges remain in capturing fast changing biological events at the relevant spatial-temporal resolution and coverage. Conventional volumetric imaging systems, such as confocal microscopy or Light Sheet Microscopy (LSM), acquire 3D volumetric images by scanning, either point by point or plane by plane across the entire volume[7,8]. While this strategy renders high resolution images, it is inherently slow due to the sequential scanning nature. Light Field Microscopy (LFM), on the other hand, obtains 3D volume in a single 2D snapshot without scanning[9–12]. This is achieved by inserting a micro-lens array (MLA) in the detection light path, recording synchronously both the spatial and angular information of the 3D sample's light field onto the 2D camera. The 3D information is then reconstructed computationally in post-processing by solving the inverse problem with knowledge of the microscope optical train[13–15]. Because of the non-scanning nature, LFM has been demonstrated to reach a high volumetric imaging speed, reaching up to 100 Hz[16–18], and opening up dynamic 3D imaging applications that are otherwise beyond the reach of scanning imaging modalities.

Currently, published LFM platforms have mainly been designed to work well for only single imaging scenarios [19–22], where the focus is to maximize the imaging performance at a particular set of volume coverage and resolution. For example, particle tracking in cell biology was achieved in a setup with high imaging resolution (~0.5 um) and small depth of view (DOV) (~6 um)[19], whereas whole-brain neural imaging in zebrafish larvae was implemented in platforms with larger DOV (~250 um) but lower resolution (~2 um)[18,22,16,17,21]. (Here, the DOV refers to the axial depth extent of the imaged volume where useful resolvable information can be collected and reconstructed.) These aforementioned examples were implemented with a specific set of hardware, lacking the flexibility to accommodate multiple imaging scenarios with diverse imaging performance requirements. This limitation has hindered the widespread adoption of LFM in biomedical research labs that do not have expertise in optics, as well as prevented the development of the LFM modality into a viable commercial product.

In this work, we developed a versatile multiscale LFM platform that enables 3D bioimaging across a diverse set of imaging scenarios, in a flexible and user-friendly manner. We were inspired by the commercial Wide Field Microscopy (WFM) design where imaging at different scales can be achieved by simply choosing different microscope objectives housed in a rotating turret. Thus, we constructed our LFM based on a commercial WFM body, with an add-on LFM detection module connected to the standard camera port, and without any modification to the main microscope body (Fig. 1a 1, Supplementary Fig. 1). By taking advantage of the rotating turret, we reasoned that a wide range of bioimaging scenarios could be met by simply switching to a different primary objective without changing other hardware components in the LFM module (Table 1). This strategy marries the versatility and ease-of-use of the inverted microscope, a workhorse in many biomedical research labs, to the unique 3D imaging capability of LFM. We selected an off-the-shelf commercially-available MLA to achieve near optimal performance for all the objectives of interest (Fig. 1b). From the user's perspective, our platform offers user-friendliness in several aspects. The sample is mounted in the same way as in an inverted WFM, and thus existing experimental workflows can be readily adopted for LFM imaging. For 3D reconstruction, we provide an open-sourced software package, along with a detailed, step-by-step procedure for acquiring and processing the experimentally measured point spread function (PSF) that is used in the reconstruction. To showcase the versatility of our LFM platform, we demonstrated its performance in three imaging scenarios that span a wide range of biologically relevant scales: characterizing whole-brain neuronal seizure in an intact zebrafish larva, recording calcium dynamic in an ex vivo mouse pancreatic islet, and observing subcellular protein dynamics in a cultured cell.

II RESULTS

A. Overview of the multiscale LFM platform.

Our multiscale LFM platform was constructed by adding a LFM module to the detection path of a commercial inverted WFM body (Methods section, Fig. 1a, Supplementary Fig. 1). The rotating nosepiece (turret) integrated in the commercial microscope body holds multiple standard primary objectives that work directly with the LFM module (Supplementary Fig 1), allowing different sets of imaging performance to be obtained by simply switching between

different primary objectives, without replacing hardware elements in the LFM arm. The LFM module is operated as an additional detection camera and is integrated into the existing image acquisition control of the WFM system.

In our platform, we implemented a recent version of LFM, termed Fourier Light Field Microscopy (FLFM)[9,11,14,15], where an MLA was inserted at the Fourier plane of the detection optical light path (Fig. 1a). The MLA sub-divides the full aperture light field from the primary objective into multiple sub-aperture light fields. Each lenslet in the MLA focuses the corresponding sub-aperture light fields onto the image plane, generating multiple angular views of the 3D sample space behind each lenslet on the detection camera. This approach allows for recording, in the same 2D snapshot, both the lateral spatial information and the angular information of the light field. The original 3D sample space is recovered after image acquisition, using a deconvolution reconstruction algorithm and the experimentally measured point spread function (PSF) of the system[14,15] . Compared to the previous version of LFM where the MLA is placed at the image plane[10,13], FLFM directly forms the angular views of a 3D sample behind each lenslet in the raw LFM image, allowing for immediate inspection and analysis on the raw LFM data without 3D reconstruction. Further, FLFM does not produce grid artifact at and near the native focal plane as observed in the previous LFM version, and has improved uniformity in lateral resolution across the DOV[11,14]. Importantly, the PSF of FLFM has lateral shift invariance, and thus the deconvolution operator in the 3D reconstruction can be performed in a parallelized fashion with GPU (Graphics Processing Unit)-accelerated Fast Fourier Transform (FFT), offering approximately 100 times faster reconstruction speed compared to the previous version of LFM[14].

To design the hardware of the LFM module, we first matched the size of the MLA to the size of the camera chip so that all the angular views formed behind the MLA can be captured onto the camera, without needing an extra optical relay, and thus maintaining design simplicity. Since we used a common scientific Complementary Metal–Oxide–Semiconductor (sCMOS) camera from Hamamatsu (ORCA-Flash4.0) with chip size of 13 × 13 mm^2, we chose a commercially-available square-shaped MLA with side length of 12 mm.

We then considered two main design parameters: the focal length of lens L2 and the number of lenslets in the MLA (Fig. 1a). The focal length of L2, denoted here as f2, was chosen to be the same with the focal length of the tube lens in the WFM (L1). This formed a 1:1 relay ratio from the back aperture of the primary objective, i.e. the Fourier plane, to the back focal plane of L2 where the MLA was placed. With the simple 1:1 relay ration, the size of the optical aperture at the MLA is the same as the size of the objective back aperture. The chosen size of the MLA, 12 x 12 mm^2, was found to be large enough to fully capture the back aperture sizes of the standard objectives used in our setup (Table 1, Supplementary Note 1). Next, we consider the number of lenslets in the MLA, which dictates the fundamental trade-off of the light field system: 3D imaging volume vs voxel resolution. For a square MLA, the number of lenslets can be represented by the linear dimension N defined as the number of lenslets on one side of the square MLA (Fig. 1a). From Supplementary Table 1 (and expanded in Supplementary Note 1), we observed that increasing N leads to a decreased Field of View (FOV) but increased DOV, as well as improved lateral and axial resolution. On the other hand, decreasing N results in an increased FOV but decreased DOV, and degraded lateral and axial resolution. These imaging performance parameters are changing in a competing fashion with respect to N. To optimize the trade-off, we evaluated how N affects two critical imaging performance metrics for 3D imaging: the size of the resolvable reconstructed single voxel, and the number of such resolvable voxels within the captured volume (defined as the product of the lateral FOV and the axial DOV). The equations to compute these two metrics are shown in Supplementary Note 1. Both metrics achieve optimality at N ~ 9, where the resolvable voxel size reaches minimum and the number of resolvable voxels reaches maximum, for all the standard primary microscope objectives (Figure 1b, c). Considering off-the-shelf commercial availability, we chose an 8 × 8 square MLA for our system. The choice for the rest of the parameters in the LFM module is detailed in Supplementary Note 1. Altogether, our design choices, and using only commercially available components, results in a LFM imaging platform that could provide optimal 3D imaging across a wide range of scales, from microns to sub-millimeters, covering cellular, tissue-level, as well as large-scale system-level imaging (Table 1).

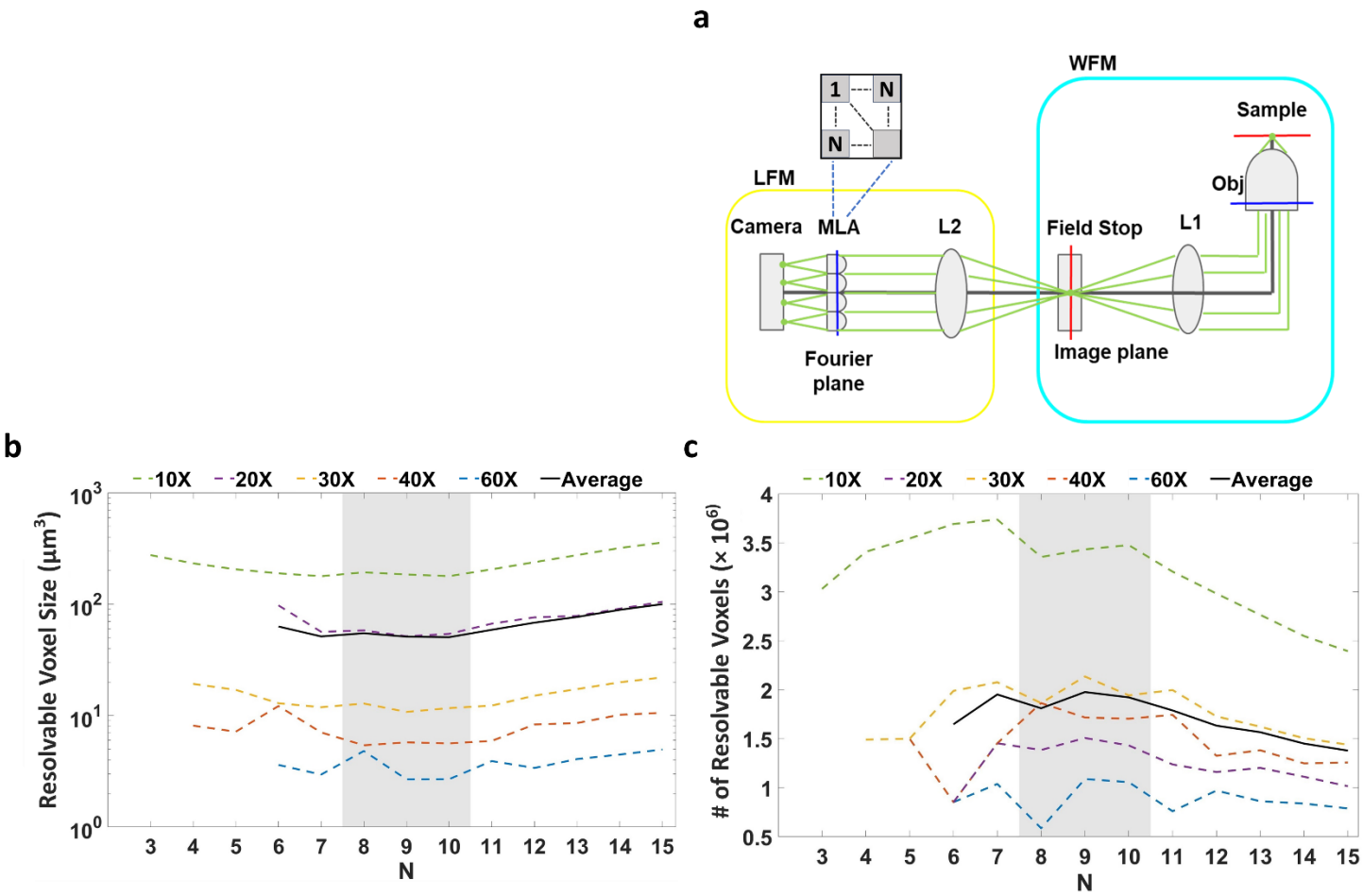

Fig. 1 Design and performance of the multiscale FLFM system. a Optical schematic of the system. Starting with the WFM body (Cyan), a field stop is placed at the standard image plane of the camera detection path. The LFM module (Yellow) consists of a relay lens L2, an MLA and a camera (Methods section). L2, in conjunction with L1 (the tube lens internal to the WFM), relays the back aperture (blue line) of the primary objective onto the MLA, which is placed at the back focal plane of L2. The camera is placed at the back focal plane of the lenslets of the MLA. Given a point source at the native object plane of WFM, the directional light ray bundle, depicted in Green, is resampled at the MLA into multiple sub-aperture ray bundles and focused into multiple focal points behind each lenslet onto the camera, representing multiple angular views of the point source. Insert, schematic for an N × N square MLA. N is defined as the linear dimension of the square MLA. **b, c** Performance of all microscope objectives of interests, represented through, respectively, the single resolvable voxel size and number of resolvable voxels, as a function of N. The objectives vary over a wide range, from 10X 0.4 NA Air to 60X 1.35 NA Oil (Table 1). The averages over all the objectives' performance curves are plotted in black. Grey regions in the plots, centered around N ~ 9, depict the optimal performance range, with the smallest resolvable voxel and largest # of resolvable voxels.

Objectives	Magnification	60	40	30	20	10
	Numerical Aperture	1.35	1.25	1.05	0.50	0.40
	Immersion Medium	Oil	Silicone Oil	Silicone Oil	Water	Air
	Refractive Index	1.51	1.41	1.41	1.33	1.00
Depth of View (μm)		21	48	87	200	780
Field of View (diameter) (μm)		140	220	290	430	860
Lateral Resolution (μm)		1.3	2.0	2.6	4.0	8.0
Axial Resolution (μm)		2.6	3.7	5.3	14	30
Imaging Scenarios		**Cell**	**Tissue & Organoid**		**System**	

Table 1. Estimated theoretical imaging performance of the multiscale FLFM system. Top orange table lists all the objectives of interest for different bioimaging applications. Bottom gray table lists the corresponding imaging performance of the LFM module using each objective. The description of theoretical performance estimation was detailed in Supplementary Note 1. As seen, with the range of standard microscope objectives depicted, the LFM module yields imaging performance that spans a wide range of spatial scale, enabling imaging across different imaging scenarios, from cellular to tissue to large-scale-system level.

B. 3D reconstruction pipeline with experimentally measured point spread function (PSF)

Richardson-Lucy (RL) deconvolution was used in our pipeline for LFM 3D reconstruction [23,24]. The algorithm uses the PSF of the system and the raw LFM image to iteratively update voxel values in the 3D sample space. We obtained the PSF experimentally by imaging a sub-resolution-limit bead the over the entire DOV. In contrast to a theoretical PSF, the experimental PSF captures the hardware imperfections deviating from the theoretical design, and thus enhances the accuracy of the 3D reconstruction[22]. For each axial plane, the PSF profile is shift invariant and the bead only needs to be imaged once at the center position[14].

A unique feature of FLFM is that, in each angular view, the centroid of the PSF changes between different axial planes, encoding both lateral and axial information in a one image. This is demonstrated in the Maximum-Intensity Projection (MIP) of the PSF with the axial position coded in different colors (Fig. 2a, b). In each angular view, different colors are distributed along a tilted line instead of overlapping over each other into a spot, as is observed for a conventional 2D imaging system, e.g. WFM. Due to the uniqueness of the FLFM PSF, none of the existing PSF extraction packages can be directly applied to the FLFM bead-imaging data. To extract the PSF from the raw bead image stack, we developed a PSF processing module that tracks the centroid of the PSF in each axial plane, ensuring an accurate and efficient cut-out of the PSF region (Supplementary Note 2). We package the PSF extraction module with the RL-deconvolution 3D reconstruction, together with additional image processing steps using Fiji [25], into an end-to-end open-source software pipeline, with a comprehensive user manual (Supplementary Software), to make our platform accessible to researchers without expert knowledge in LFM.

The RL-deconvolution 3D reconstruction was implemented with GPU acceleration, carried out on a standard desktop workstation (Supplementary XXX). Supplementary Table 3 listed the reconstruction times for all the datasets shown in sections D, E, F. Briefly, with our computing hardware, it takes ~ 20 s to reconstruct a 2D (2048x2048) raw LFM image into a 3D volume. Supplementary Note 2 discusses practical ways to speed up the reconstruction process, such as down sampling the raw data (and sacrificing resolution), boosting the GPU processing power, or utilizing cloud computing services.

C. Resolution characterization.

We characterized the resolution of the LFM system by measuring the Full Width Half Maximum (FWHM) of the reconstructed single-bead images in both lateral and axial dimensions (Fig. 2, Supplementary Fig. 2). Since the PSF is acquired from imaging a sub resolution-limit single bead, each slice of the 3D PSF is equivalent to a LFM image of a single bead positioned at a different axial depth. Therefore, to reconstruct a single bead at different axial plane, we simply need to reconstruct several single slices from the PSF stack, below and above the native focal plane, using the full 3D PSF. We reconstructed five single-bead images, for each of the 10x, 20x, and 60x primary objectives. The lateral and axial FWHM values are found to be, respectively: 5.8 ± 0.1 µm, 31.0 ± 1.0 µm (10x objective); 1.8 ± 0.3 µm, 5.5 ± 0.2 µm (30x objective); 0.9 ± 0.04 µm, 3.2 ± 0.13 µm (60x objective) (Fig. 2c-d, Supplementary Fig. 2). For all three objectives, the FWHM measurements generally matched the theoretically-estimated lateral and axial resolution shown in Table 1. Notably, the lateral FWHM showed ~ 30% improvement over the theoretically-estimated values (Fig. 2d). This is in fact not unexpected, as deconvolution has been shown to provide better lateral resolution performance than theoretical estimates based on wave-optics approximations[22]. Overall, the experimentally-measured imaging resolutions show that with the three objectives considered, the LFM provides the performance suitable for three different biological imaging scenarios: low-resolution large-volume system scale with the 10x, cellular-resolution medium-volume tissue scale with the 30x, and subcellular-resolution few-cells scale with the 60x. These imaging scenarios are demonstrated in the following sections.

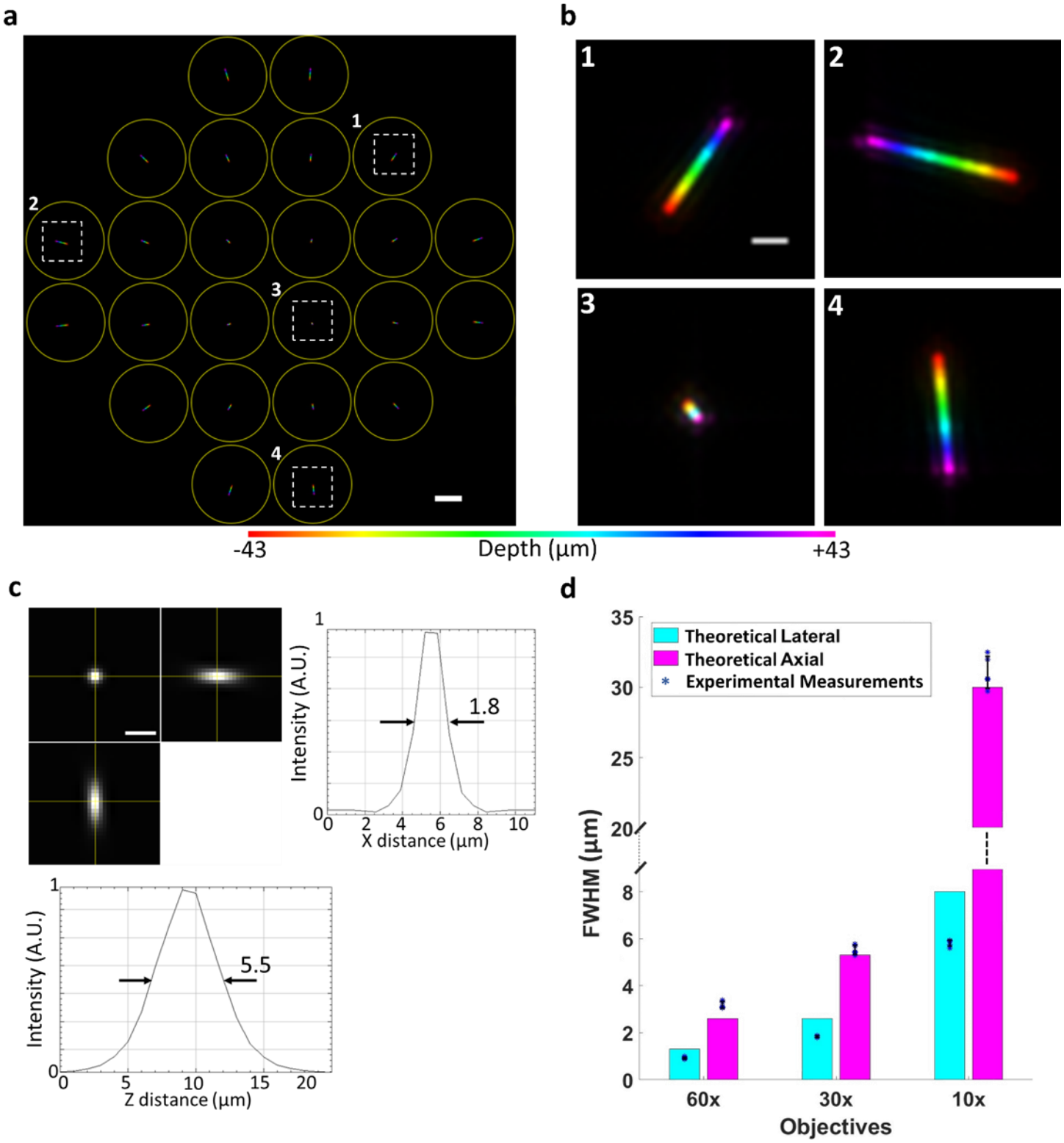

Fig. 2 Resolution characterization of the multiscale LFM. a Axial maximum-intensity projection of the PSF, taken with 30x 1.05 NA silicone oil immersion objective, where the axial z-position is color-coded over the DOV from -43 µm to 43 µm. The angular views behind each lenslet are circled out in yellow. Only the central views of the square MLA that are fully within the circular aperture of the objective are shown. **b** Zoomed-in views of dashed white boxes in **a**. Different angular views are seen as encoding z-depth (as colors) along lines oriented at different angles. **c** Lateral and axial image and line profiles of a reconstructed bead, recorded with the 30x objective. See Supplementary Fig. 2 for the corresponding image and line profiles for the 60x and 40x objectives. A.U., Arbitrary Unit. **d** FWHM measurements compared to theoretical estimates of the resolutions, for the three objectives shown. FWHM of five reconstructed beads were measured and

plotted individually as asterisks (*). The FWHM averages are shown as solid dots, and the error bars show the standard deviations. Theoretical estimates of the lateral and axial resolution are presented as cyan and magenta columns, respectively (Table 1). Overall, experimental resolution values agreed, and exceeded, theoretical estimates (see text for details). Scale bars, (**a**) 100 µm, (**b**) 10 µm, (**c**) 5 µm.

D. Imaging whole-brain seizures in zebrafish

We demonstrated the ability of our multiscale LFM in capturing fast biological system-level dynamics through imaging whole-brain seizures in larval zebrafish. Seizures are large-scale whole-brain neuronal population activity that unfolds within several seconds. Capturing the whole-brain seizure events in the zebrafish requires both fast imaging speed as well as a large imaging volume. Using the 10x objective (Table 1), we imaged the whole brain volume of ~ 500 × 800 × 300 (XYZ) μm^3 at 30 volumes/s (Supplementary Video 1), significantly faster than the state-of-the-art seizure imaging achieved by LSM operated at ~5 volumes/s[26]. Even though seizure events in zebrafish generally last a few seconds to minutes [27,28], the high volumetric imaging speed allows for capturing of the fast dynamics within each event, especially during the rapid onset window. By analyzing the time series data from a cropped-out single lenslet image, which has data size at two orders of magnitude smaller than the full dataset, we could identify the existence and precise timing of the seizure event - this is an important capability to facilitate experimental trouble-shooting and efficient analysis of the large datasets. In this experiment, we reconstructed a 14-second movie for one representative seizure event (Fig. 3a, b). The averaged intensity over the reconstructed whole brain provides a coarse description of the seizure temporal profile (Fig. 3c). To highlight the propagation of brain activity across the brain during the seizure onset, we performed a temporal difference analysis on the 3D reconstructed movie (Methods). The temporal difference was computed from subtracting the previous time point intensity from the current time point intensity for each reconstructed voxel and setting the negative intensity to zero. From the temporal difference movie, we were able to observe clearly the seizure onset window, from initiation to propagation throughout the whole brain (Fig. 3d, Supplementary Video 1). The achieved imaging contrast and resolution allowed us to clearly discern the seizure activation and propagation across the various brain regions. We surmise that in future studies, the low-resolution but high volume-coverage and high-speed LFM described here could be effectively combined with other high-resolution imaging modalities, such as LSM or confocal microscopy, where LFM provides the targeted regions of interests for the latter modalities to focus the investigations on.

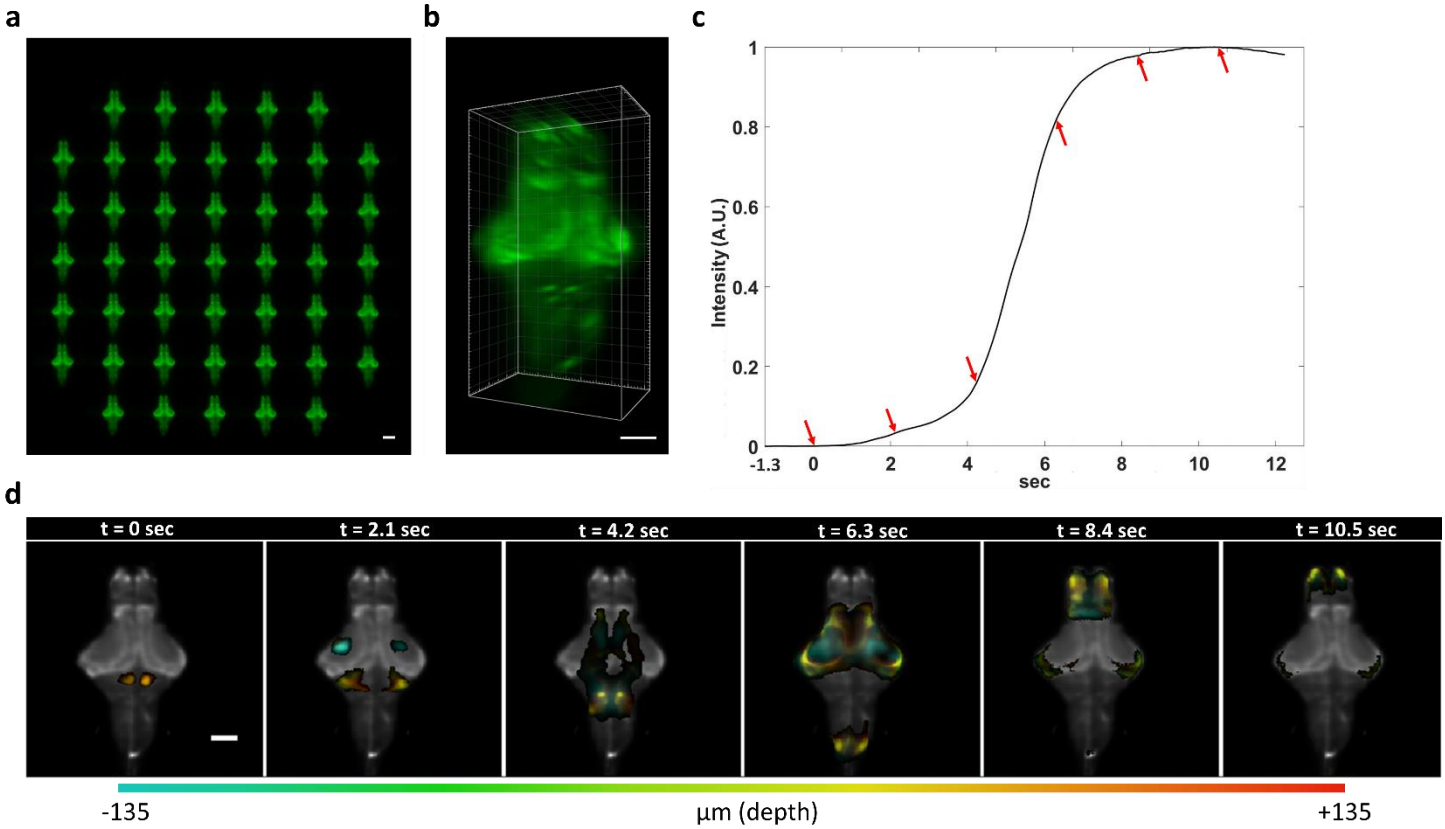

Fig. 3 Imaging seizure in zebrafish whole brain with FLFM. The fish, expressing a pan neuronal GCamp7f calcium indicator (HuC::GCaMP7f), was immobolized in agarose and the seizure was chemically induced by administering 15mM PTZ (Method). The imaging is performed using 10x 0.4 NA oil immersion as the primary objective. The calcium activity was recorded at 30 volumes/s over a volume size of ~860 × 860 × 270 μm^3. **a** One timeframe of FLFM recording shows different angular views of the fish brain. **b** 3D Reconstruction of **a** rendered in 3D. The reconstructed volume has 27 z slices with each z slice of 10 µm. The rendering shows the active neurons located in different areas of the brain. **c** Averaged intensity in the brain region traced over time during one seizure event. Red arrows, time points at 2.1 sec apart with the first arrow pointing at the seizure. A.U., Arbitrary Unit. **d** Depth color-coded temporal difference intensity (Method) at the time points in **c**. The seizure initialized (t = 0 sec) in the cerebellum area of the fish brain, spread out along both rostral and caudal directions. Gray scale, the average intensity over time and over axial direction presented as a contrast for the dynamical intensity. Scale bars, a 100 µm, b 100 µm, d 100 µm.

E. Imaging calcium dynamics in mouse pancreatic islet

Calcium signaling is critical in how beta cells in pancreatic islets response to glucose, as part of their central role in maintaining glucose homeostasis and overall metabolic health[29–31]. It is generally understood that upon sensing glucose concentration above a certain threshold, beta cells in an islet spike up their intracellular calcium levels, which then kickstart a cascade leading to insulin synthesis and secretion[32–38]. Questions remain, however, on how individual beta cells coordinate their calcium activation to achieve the whole-islet response. Past imaging studies[32–38], using conventional imaging modalities (e.g. confocal microscopy or LSM), have not resolved these questions as they lack the necessary volumetric imaging speed, topping out at ~ 1 volumes/s to cover the entire islet[34], while the intrinsic cellular calcium dynamic happens at sub-second time scale[39,40]. Thus, there is a need for an imaging solution that could capture calcium dynamics in the entire 3D islet at volumetric rate higher than what conventional techniques could provide, to ensure that the dynamic signals are captured faithfully.

The fast 3D imaging capability of LFM provides a solution for the above challenge. Using the 30x objective, we imaged an entire mouse islet, where the beta cells were labeled with the calcium indicator GCamp6f, in 11 mM glucose concentration, at 20 volumes/s, covering the entire volume of the islet of ~ 100 x 100 x 86 (XYZ) μm^3 (Methods). As shown in a representative 70-second recording (Fig. 4a, b, Supplementary Video 2), we captured the fast calcium dynamics that spontaneously initiated in a sub-region then spread in 3D across the entire islet. From the spatially-integrated intensity trace over time (Methods), we observe that the islet, as a whole, underwent repetitive calcium activation events (Fig. 4c). Within each activation event, lasting for ~ few seconds, the fast 3D imaging speed of LFM revealed a complex spatiotemporal calcium dynamic that evolved at sub-second scale across the 3D volume of the islet. Focusing on three representative activation events, and representing the calcium dynamic through the temporal difference intensity (Fig. 4d), we observe that the three calcium events initiated at different locations in the islet, then the activation spread across the islet in different 3D patterns. The observed heterogeneity in where the calcium events initiated, and how they propagated across the islet, highlights the benefits of LFM in providing the necessary fast volumetric imaging speed to capture these complex spatiotemporal dynamics. We envision our LFM platform would be the ideal imaging tool in future studies aimed at more in-depth and functional characterization of the pancreatic islet calcium dynamics, e.g. in response to changing glucose levels, and/or in concurrent recordings of insulin synthesis and release.

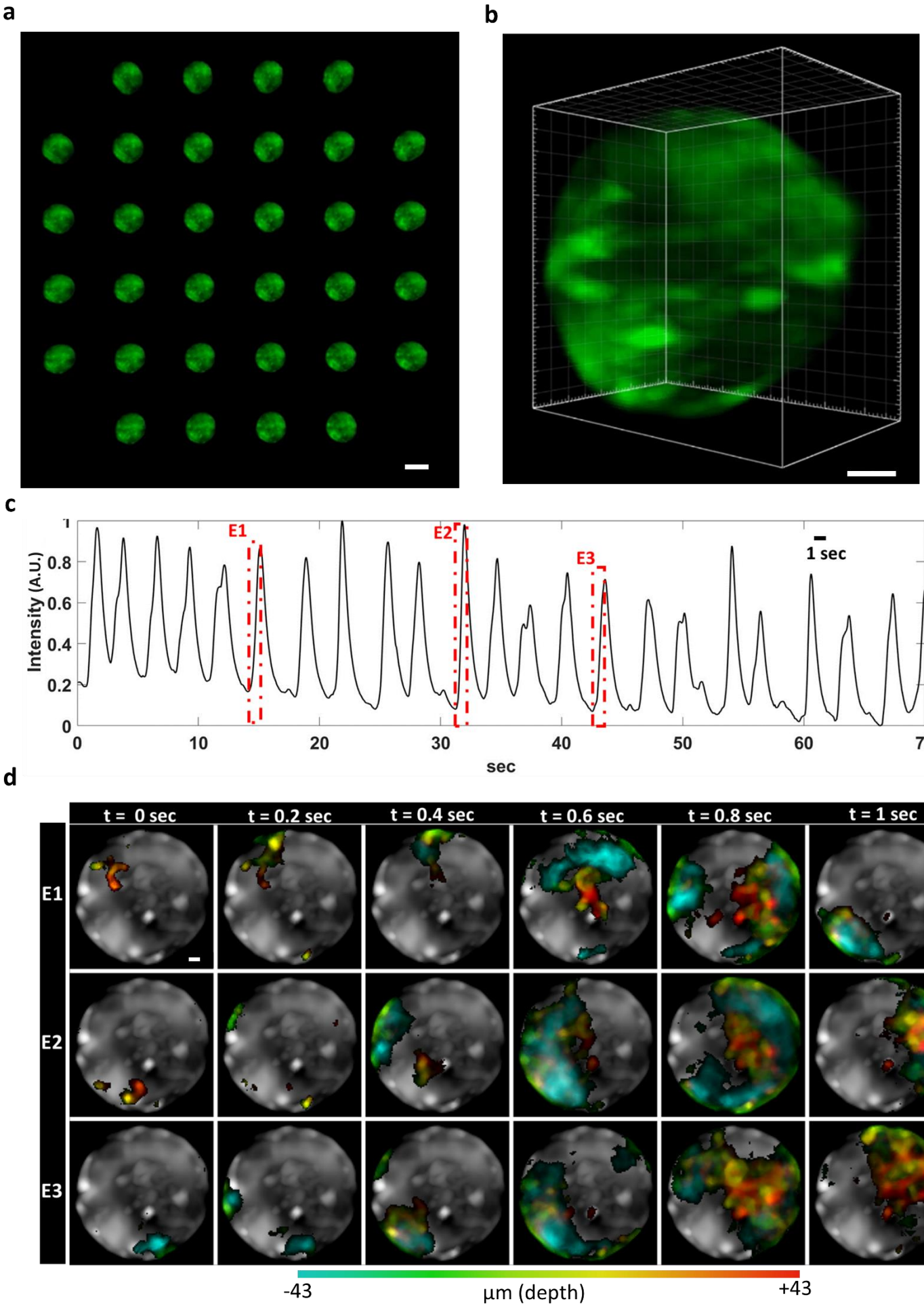
a
b
c
E1
E2
E3
1 sec
Intensity (A.U.)
0
0.2
0.4
0.6
0.8
1
0
10
20
30
40
50
60
70
sec
d
t = 0 sec
t = 0.2 sec
t = 0.4 sec
t = 0.6 sec
t = 0.8 sec
t = 1 sec
E1
E2
E3
-43
µm (depth)
+43

Fig. 4. Imaging calcium dynamics in mouse pancreatic islets. Functional imaging of a mice islet with calcium indicator GCaMP6f expressed in pancreatic beta cells. The islet was in equilibrium with 11 mM glucose concentration. Imaging was performed using the 30x 1.0 NA Silicone Oil objective, recorded at 20 volumes/s. **a** Single image frame of raw LFM recording, showing the different angular views of the islet. **b** Reconstruction of **a** rendered in 3D. The reconstructed volume has 43 z-slices separated by 2 µm/slice. **c** Temporal evolution of the fluorescence intensity, averaged over the entire islet. Red dashed boxes indicate the 1-second onset window of three representative calcium events (E1, E2, E3) that are analyzed further in **d**. A.U., Arbitrary Unit. **d** Depth color-coded images, of the temporal difference intensity (Methods), at six time points for calcium event E1, E2, E3 in **c**. The sequential time points are arranged horizontally, while the calcium events are separated vertically. As seen, each event initiated at a different 3D location (t = 0 sec) and propagated through the islet in different spatial patterns. The average-intensity-projection over both time and z-depth is shown as the gray-scale image in the background, for each of E1, E2, E3, to provide spatial context for the entire islet. Scale bars, **a** 100 µm, **b** 20 µm, **d** 10 µm.

F. Imaging protein dynamics in live cultured cells

Toward the finer scale, we demonstrate subcellular imaging with our LFM platform, through imaging protein dynamics in live cultured cells with the 60x objective. Fig. 5 shows our results in imaging a live Human Bone Osteosarcoma Epithelial cell (U2OS line) expressing the fluorescent protein mNeonGreen fused to the human prolactin receptor (hPRLR) (Methods). The hPRLR protein plays a crucial role in various physiological processes and related diseases, including breast cancer, autoimmune disease, and metabolic disorders [41–44]. Understanding hPRLR dynamics is essential for advancing knowledge in these areas.

In the imaging experiment, we captured the rapid movement of the fluorescently-labeled hPRLR proteins throughout the cell's volume, at volumetric speed of 20 volumes/s, over the volume of ~ 50 × 50 × 17 (XYZ) μm^3(Fig. 5a, b, Supplementary Video 3). Note that both the fast volumetric imaging rate of LFM and the sub- to few-micron 3D resolution achieved with the 60x objective (Table 1, Supplementary Fig. 3) were critical in this imaging scenario. High-speed or high-resolution imaging alone will not be able to faithfully resolve the dynamic movements of the subcellular protein puncta throughout the cell (Fig. 5c, d, e, f).

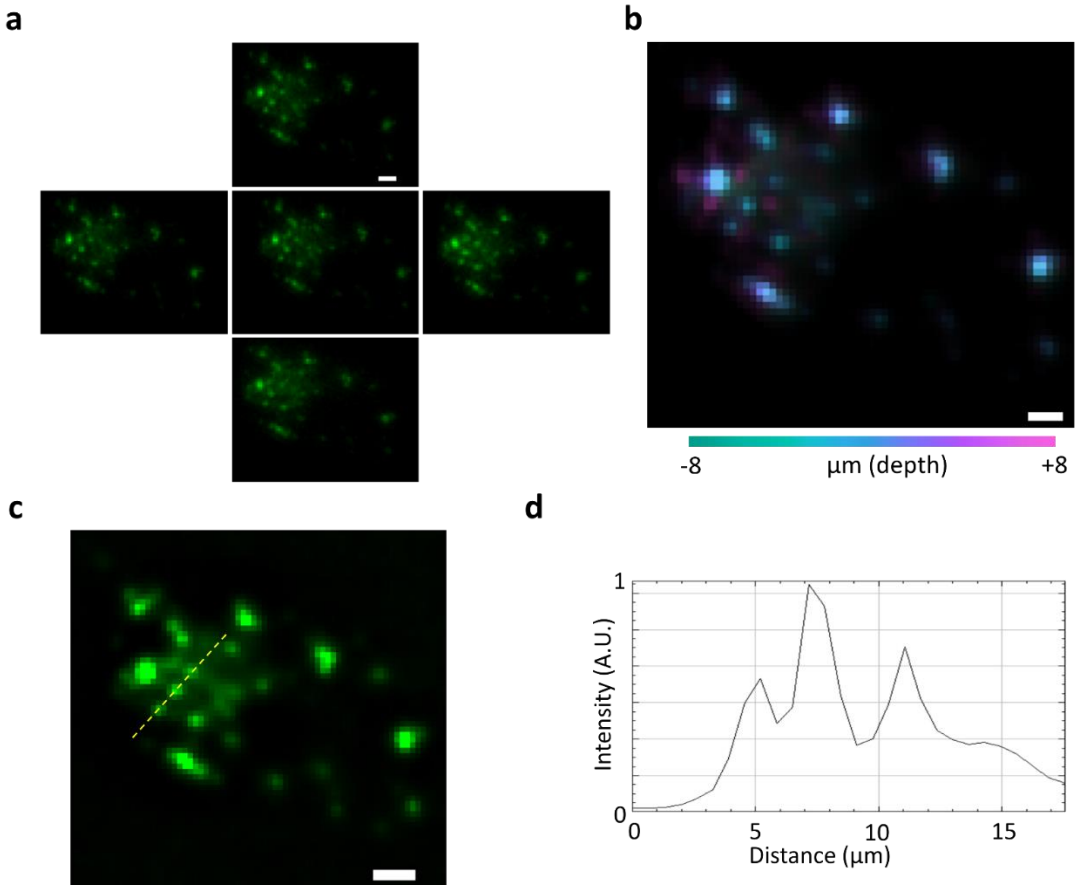

Fig. 5. Imaging protein dynamics in live cultured cells. The Human Bone Osteosarcoma Epithelial cell (U2OS line) expressed the fluorescent protein mNeonGreen fused to the human prolactin receptor (Methods). Imaging was performed using the 60x 1.35 NA Oil objective (Table 1), recorded at 20 volumes/s (Supplementary Video 3). **a** Single image frame of the raw LFM recording, showing different angular views of the cultured cell. **b** 3D reconstruction of **a**, shown with color-coded z-depth. The reconstructed volume has 17 z-slices separated by 1 µm/slice. **c** One z-slice at +1 µm from the reconstructed volume in **b**. **d** Line profile of the yellow line in **c**, demonstrating the micron-level resolution in distinguishing the labeled protein puncta. A.U., Arbitrary Unit. Scale bars, 5 µm.

III. DISCUSSION & CONCLUSION

In summary, we have presented a versatile multiscale LFM platform that is easily accessible to biological researchers. By integrating a LFM detection module with a conventional commercially available wide field microscope, we demonstrate the versatility of our LFM system, enabling observation of various 3D dynamical processes across many scales, ranging from sub-cellular protein dynamics to intercellular calcium signaling in ex vivo tissues, to whole-brain neural activity of an intact animal. The built-in flexibility and ease of use of the commercial microscope makes the LFM module accessible and user-friendly. While we built our platform on an inverted microscope body, for flexible adaptability to cells and tissues samples, the LFM module could similarly be added to an upright microscope, for applications that are more suited to that imaging configuration, such as neuroimaging. Instead of a wide field microscope, LFM can also be integrated in a similar manner with other 2D imaging systems, such as a confocal microscope or LSM, to provide an option for fast, lower-resolution synchronous volumetric imaging, to complement the existing slower, higher-resolution imaging capability of those systems. In particular, the integration of LFM with LSM enables selective volume illumination microscopy (SVIM)[45,46], which has been shown to improve contrast and effective resolution over wide field illumination. In the work presented here, we have aimed to balance the competing needs of maximizing imaging performance versus minimizing the complexity and cost of the LFM module, thus opting for simplified optical configurations and off-the-shelf parts. If high imaging performance is the priority, different design and component choices could be made. For example, the resolution and imaging volume of the multiscale LFM platform could be enhanced with a customized MLA, with application-specific optical parameters and/or complex multi-focal features[22]. A filter-wheel-like device could be used to house different MLA's with different specifications, thus allowing for switching in specific MLAs to match particular imaging applications. Performance enhancements could also come from a larger camera sensor size with higher pixel counts, allowing for either more angular views to be captured or higher pixel sampling rate. Further optical magnification or de-magnification could be implemented between the MLA and camera to make full use of the camera chip size, realizing the true optical resolution limit. As computing power continues to advance, our versatile multiscale LFM platform has the potential to reach more researchers and provides fast 3D imaging solutions to a broad range of biological applications, empowering scientists to explore more biological questions and unlock new working principles of living systems.

ACKNOWLEDGEMENTS

We thank Dr. Amina Kinkhabwala (California Institute of Technology) and Dr. David Prober (California Institute of Technology) for protocols sharing and initial consultation for the zebrafish experiment. We thank Dr. Kate White (University of Southern California) for inputs to the mouse islet experiment.

Reference:

1. Schneckenburger, H. & Richter, V. Challenges in 3D Live Cell Imaging. *Photonics* **8**, 275 (2021).
2. Muldoon, S. F. & Bassett, D. S. Network and Multilayer Network Approaches to Understanding Human Brain Dynamics. *Philos. Sci.* **83**, 710–720 (2016).
3. Palm, G. Neural Information Processing in Cognition: We Start to Understand the Orchestra, but Where is the Conductor? *Front. Comput. Neurosci.* **10**, 3–3 (2016).
4. Saleem, S. & Kannan, R. R. Zebrafish: an emerging real-time model system to study Alzheimer's disease and neurospecific drug discovery. *Cell Death Discov.* **4**, 45–45 (2018).
5. Morgan, V. L., Abou-Khalil, B. & Rogers, B. P. Evolution of functional connectivity of brain networks and their dynamic interaction in temporal lobe epilepsy. *Brain Connect.* **5**, 35–44 (2015).
6. Zhang, Z. *et al.* Dynamic functional connectivity and its anatomical substrate reveal treatment outcome in first-episode drug-naïve schizophrenia. *Transl. Psychiatry* **11**, 282–282 (2021).
7. Elliott, A. D. Confocal Microscopy: Principles and Modern Practices. *Curr. Protoc. Cytom.* **92**, e68–e68 (2020).
8. Stelzer, E. H. K. *et al.* Light sheet fluorescence microscopy. *Nat. Rev. Methods Primer* **1**, (2021).
9. Scrofani, G. *et al.* FIMic: design for ultimate 3D-integral microscopy of in-vivo biological samples. *Biomed. Opt. Express* **9**, 335–346 (2017).
10. Levoy, M., Ng, R., Adams, A., Footer, M. & Horowitz, M. Light field microscopy. *ACM Trans. Graph.* **25**, 924–934 (2006).
11. Llavador, A., Sola-Pikabea, J., Saavedra, G., Javidi, B. & Martínez-Corral, M. Resolution improvements in integral microscopy with Fourier plane recording. *Opt. Express* **24**, 20792 (2016).
12. Kim, K. Single-Shot Light-Field Microscopy: An Emerging Tool for 3D Biomedical Imaging. *BioChip J.* **16**, 397–408 (2022).
13. Broxton, M. *et al.* Wave optics theory and 3-D deconvolution for the light field microscope. *Opt. Express* **21**, 25418–25439 (2013).
14. Guo, C., Liu, W., Hua, X., Li, H. & Jia, S. Fourier light-field microscopy. *Opt. Express* **27**, 25573–25594 (2019).
15. Galdón, L., Saavedra, G., Garcia-Sucerquia, J., Martínez-Corral, M. & Sánchez-Ortiga, E. Fourier lightfield microscopy: a practical design guide. *Appl. Opt.* **61**, 2558 (2022).

16. Pégard, N. C. *et al.* Compressive light-field microscopy for 3D neural activity recording. *Optica* **3**, 517 (2016).

17. Yoon, Y.-G. *et al.* Sparse decomposition light-field microscopy for high speed imaging of neuronal activity. *Optica* **7**, 1457 (2020).

18. Zhang, Z., Cong, L., Bai, L. & Wang, K. Light-field microscopy for fast volumetric brain imaging. *J. Neurosci. Methods* **352**, 109083 (2021).

19. Sims, R. R. *et al.* Single Molecule Light Field Microscopy. (2020) doi:10.1101/2020.05.20.104802.

20. Shaw, M. *et al.* Three-dimensional behavioural phenotyping of freely moving C. elegans using quantitative light field microscopy. *PloS One* **13**, e0200108–e0200108 (2018).

21. Prevedel, R. *et al.* Simultaneous whole-animal 3D imaging of neuronal activity using light-field microscopy. *Nat. Methods* **11**, 727–730 (2014).

22. Cong, L. *et al.* Rapid whole brain imaging of neural activity in freely behaving larval zebrafish (Danio rerio). *eLife* **6**, e28158 (2017).

23. Lucy, L. B. An iterative technique for the rectification of observed distributions. *Astron. J.* **79**, 745 (1974).

24. Richardson, W. H. Bayesian-Based Iterative Method of Image Restoration*. *J. Opt. Soc. Am.* **62**, 55 (1972).

25. Schindelin, J. *et al.* Fiji: an open-source platform for biological-image analysis. *Nat. Methods* **9**, 676–682 (2012).

26. de Vito, G. *et al.* Fast whole-brain imaging of seizures in zebrafish larvae by two-photon light-sheet microscopy. *Biomed. Opt. Express* **13**, 1516–1536 (2022).

27. Cho, S.-J. *et al.* Zebrafish as an animal model in epilepsy studies with multichannel EEG recordings. *Sci. Rep.* **7**, 3099–3099 (2017).

28. Gawel, K. *et al.* Seizing the moment: Zebrafish epilepsy models. *Neurosci. Biobehav. Rev.* **116**, 1–20 (2020).

29. Klec, C., Ziomek, G., Pichler, M., Malli, R. & Graier, W. F. Calcium Signaling in ß-cell Physiology and Pathology: A Revisit. *Int. J. Mol. Sci.* **20**, 6110 (2019).

30. Rorsman, P. & Ashcroft, F. M. Pancreatic β-Cell Electrical Activity and Insulin Secretion: Of Mice and Men. *Physiol. Rev.* **98**, 117–214 (2018).

31. Podobnik, B. *et al.* β Cells Operate Collectively to Help Maintain Glucose Homeostasis. *Biophys. J.* **118**, 2588–2595 (2020).

32. Zmazek, J. *et al.* Assessing Different Temporal Scales of Calcium Dynamics in Networks of Beta Cell Populations. *Front. Physiol.* **12**, 612233–612233 (2021).

33. Kravets, V. *et al.* Functional architecture of pancreatic islets identifies a population of first responder cells that drive the first-phase calcium response. *PLoS Biol.* **20**, e3001761–e3001761 (2022).

34. Zhao, J. *et al.* In vivo Imaging of Calcium Activities from Pancreatic β-cells in Zebrafish Embryos Using Spinning-disc Confocal and Two-photon Light-sheet Microscopy. *Bio-Protoc.* **11**, e4245–e4245 (2021).

35. Zhao, J. *et al.* In vivo imaging of β-cell function reveals glucose-mediated heterogeneity of β-cell functional development. *eLife* **8**, e41540 (2019).

36. Akalestou, E. *et al.* Intravital imaging of islet Ca(2+) dynamics reveals enhanced β cell connectivity after bariatric surgery in mice. *Nat. Commun.* **12**, 5165–5165 (2021).

37. Lavagnino, Z. *et al.* Snapshot Hyperspectral Light-Sheet Imaging of Signal Transduction in Live Pancreatic Islets. *Biophys. J.* **111**, 409–417 (2016).

38. Kenty, J. H. R. & Melton, D. A. Testing pancreatic islet function at the single cell level by calcium influx with associated marker expression. *PloS One* **10**, e0122044–e0122044 (2015).

39. Zhang, Y. *et al.* Fast and sensitive GCaMP calcium indicators for imaging neural populations. *Nature* **615**, 884–891 (2023).

40. Chen, T.-W. *et al.* Ultrasensitive fluorescent proteins for imaging neuronal activity. *Nature* **499**, 295–300 (2013).

41. Gorvin, C. M. The prolactin receptor: Diverse and emerging roles in pathophysiology. *J. Clin. Transl. Endocrinol.* **2**, 85–91 (2015).

42. Kavarthapu, R. & Dufau, M. L. Prolactin receptor gene transcriptional control, regulatory modalities relevant to breast cancer resistance and invasiveness. *Front. Endocrinol.* **13**, 949396–949396 (2022).

43. Costanza, M., Binart, N., Steinman, L. & Pedotti, R. Prolactin: A versatile regulator of inflammation and autoimmune pathology. *Autoimmun. Rev.* **14**, 223–230 (2015).

44. Wu, T. *et al.* A Century of Prolactin: Emerging Perspectives as a Metabolic Regulator. *Diabetes Metab. Res. Rev.* **40**, (2024).

45. Truong, T. V. *et al.* High-contrast, synchronous volumetric imaging with selective volume illumination microscopy. *Commun. Biol.* **3**, 74–74 (2020).

46. Keomanee-Dizon, K., Fraser, S. E. & Truong, T. V. A versatile, multi-laser twin-microscope system for light-sheet imaging. *Rev. Sci. Instrum.* **91**, 053703–053703 (2020).

Methods

Hardware setup. The optical setup was composed of two subsystems: the commercial WFM (Olympus, IX83 Inverted Microscope) and the customized LFM module (Supplementary Fig. 1). The WFM is equipped with a fluorescence light source (Olympus, U-HGLGPS) and standard filter cube sets for different colors. The customized LFM module was appended to the left camera port of the WFM body. In the LFM module, a field stop was placed at the image plane to control the size of the field of view so that the images formed behind adjacent lenslets do not overlap each other[1–3]. As depicted in Fig. 1a, relay lens L2, with focal length = f_2, was positioned at distance f_2 behind the field stop, and the MLA was placed at distance f_2 from L2. Coupled with the WFM internal tube lens L1, the relay lens L2 relayed the back aperture plane (i.e. Fourier plane) of the primary objective onto the MLA. A sCMOS camera (Hamamatsu, ORCA-Flash4.0) was placed at the back focal plane of the lenslets where the different angular views of the 3D sample were formed. For imaging in LFM mode, the fluorescence signal was directed to the left camera port in the WFM system. The emission light in all three biological samples were in the green band and thus imaged with a FITC filter cube set (Olympus, U-FF). Image acquisition was controlled by Micro-Manager[4]. A photograph of the hardware setup is shown in Supplementary Fig. 1. The key hardware components, with their specifications, are summarized in Supplementary Table 1.

Zebrafish imaging experiment. *Animal model*: All zebrafish procedures were approved and completed according to the guidelines set by the University of Southern California Department of Animal Research. Zebrafish larvae in the *casper* background with pan-neuronal GCaMP7f expression, *Tg(elavl3:GCamp7f)* (gift from Dr. David Prober, California Institute of Technology), were imaged at 5 days post-fertilization. *Zebrafish preparation*: The zebrafish was paralyzed in a petri dish with 30 μL of α-bungarotoxin (MilliporeSigma, #203980) solution, at concentration of 1 mg/mL in E3 medium (5 mM NaCl, 0.17 mM KCl, 0.33 mM CaCl2, 0.33 mM MgSO4), for 30 seconds. Then 3 mL of E3 was added and the petri dish was covered in tin foil and left inside a 28°C incubator for 30 minutes. Subsequently the zebrafish was washed with 3 mL of E3 for three times, then anesthetized by placing into tricaine solution (0.05% tricaine in E3; MS 222, Sigma-Aldrich, #E10521) for a a few minutes before it was ready to be mounted for imaging. *Fish mounting:* The zebrafish was mounted in a #1.5 coverglass-bottom petri dish (MatTek, P35G-1.5-10-C), in 1.8 mL of agarose solution (1.5% agarose in E3, with 0.05% tricaine) (Thermo Fisher Scientific, UltraPure Low Melting Point Agarose, #16520100), with its dorsal side facing down and pushed as close to the bottom of the petri dish as possible. This is done to ensure the most direct optical path of the microscope objective to the brain with the inverted microscope used in the experiment. Once the agarose has solidified, the tricaine was washed out by adding and removing 3 mL of E3 for three times, with 5 minutes of equilibration time between washes. After the last wash, 1.155 mL of E3 was added. The sample petri dish was then placed in the stage-top incubator of the microscope, with the temperature set to 28°C, and left to equilibrate for at least 15 minutes. *Imaging seizures induced by pentylenetetrazole (PTZ)*: Aliquots of 45 μL (1 M) PTZ (Cayman Chemical, #18682) was made with E3 and kept frozen until use. After equilibration in the stage-top incubator, the sample was adjusted to be in the desired microscope field of view, and the focal plane was adjusted to be at ~ 150 μm into the zebrafish brain from the dorsal surface, with microscope objective 10x 0.4 NA Air. One minute before the start of the timelapse, 45 μL (1 M) of PTZ (thawed and brought to 28°C) was added to the sample petri dish, allowing the time for closing the lid of the incubator. Timelapse was recorded for 90 minutes, with exposure time of 33.3 ms, resulting in a volumetric imaging rate of 30 volumes/s.

Mouse islet imaging experiment. *Animal Model:* All mouse procedures were approved and completed according to the guidelines set by the Children's Hospital of Los Angeles Institutional Animal Care and Usage Committee. Ins1Cre-GCaMP6f, β cell-specific GCaMP6f protein expression, were generated by crossing Ins1Cre mice (The Jackson Laboratory, #026801) and Ai95(RCL-GCaMP6f)-D mice (The Jackson Laboratory, #028865), both on a C57Bl/6J background. *Islet Isolation and dissociation:* Islets were isolated using a 3.5 mg/mL liberase and 1.5 mg/mL DNAse enzyme blend (Roche Diagnostics) as previously described[5]. Briefly, the enzyme solution was perfused into the pancreas via the bile duct, and the inflated pancreas was removed for further digestion at 37 °C for 12 min. Extracted islets were hand-picked under a fluorescence

light microscope to isolate Ins1Cre-GCaMP6f islets and incubated with Roswell Park Memorial Institute (RPMI) 1640 (Gibco). Islets were transferred into an 8-well #1.5 coverglass-bottom imaging chamber (Ibidi, #80826) with RPMI 1640 and left at 37°C overnight before being used for experiments. On the day of imaging, islets were equilibrated in Kreb's Ringer bicarbonate buffer as previously described[5] at 2.8 mM basal glucose concentration, and then increased to 11 mM static glucose incubation. *Imaging*: The islet sample was placed in the microscope stage-top incubator, with temperature set to 37°C, and positioned at the center of the field of view. The focal plane was adjusted to be at the center of the islet along the z-direction, with microscope objective 30x 1.0 NA Silicone Oil. Timelapse was recorded for 70 seconds, with exposure time of 50 ms, resulting in a volumetric imaging rate of 20 volumes/s.

Cell imaging experiment. *Plasmid design:* A plasmid containing human prolactin receptor (hPRLR), fused to the rat PRLR signal peptide, was obtained as a gift from Vincent Goffin (INSERM, Paris, France). pcDNA3 Flag HA (#10792) plasmid was obtained from Addgene. The rat PRLR signal peptide, hPRLR and the fluorescent protein mNeonGreen were cloned into the pcDNA3 plasmid using Takara In-Fusion Snap Assembly (#638947) according to the manufacturer's protocol, such that mNeonGreen was fused to the C-terminus of hPRLR. U2OS cells were acquired from the American Type Culture Collection (Manassas, VA). *Cell culture*: Cells were cultured in DMEM (Corning, #10-013-CV), supplemented with 10% fetal bovine serum (Thermo Fisher Scientific, #A5256701), 1% penicillin/streptomycin (Thermo Fisher Scientific, #15140122), and 1% L-glutamine (Sigma-Aldrich, #G7513). For imaging experiments, cells were grown to ~ 80% confluency before being seeded onto 8-well #1.5 coverglass-bottom imaging chamber (Ibidi, #80807). Twenty-four hours after seeding, transient transfection of the pcDNA3-hPRLR-mNeonGreen plasmid was performed using Lipofectamine 3000 and P3000 reagents (Thermo Fisher Scientific, #L30008) according to the manufacturer's protocol. Twenty-four hours after transfection, cell culture medium was replaced with phenol red-free Leibovitz's L-15 medium (Thermo Fisher Scientific, #21083027) for imaging. *Imaging*: The cell sample was placed in the microscope stage-top incubator, with temperature set to 37°C, and positioned at the center of the field of view. The focal plane was adjusted to be coincident with the cell, achieving the sharpest view of the sample, with microscope objective 60x 1.35 NA Oil. Timelapse was recorded for 50 seconds, with exposure time at 50 ms, resulting in a volumetric imaging rate of 20 volumes/s.

Richardson-Lucy (RL) deconvolution. The LFM 3D reconstruction problem was solved using RL deconvolution method as described previously[6–8]. Briefly, if we arrange both the 2D image space and the 3D voxel space into vectors, the light field imaging system can be written as a matrix vector multiplication wrapped by a Poisson noise model. We denote $\vec{g}$ as the vectorized 3D volume, $\vec{f}$ as the vectorized raw experimentally recorded 2D light field image, $Pois\{\cdot\}$ as the Poisson process and $\mathbf{H}$ as the PSF matrix where each column is the PSF of each voxel. The forward image formation process is characterized by the following equation:

$$\vec{f} \sim Pois\{\mathbf{H} \cdot \vec{g}\} \tag{1}$$

The PSF matrix $\mathbf{H}$ is acquired from the experimentally measured PSF, through imaging of sub-diffraction fluorescent beads. The goal of the reconstruction is to solve for the unknown vector $\vec{g}$. RL deconvolution was developed to solve this problem[9,10]. The deconvolution algorithm starts with an initial guess of $\vec{g}$, then iteratively updates the entry values in $\vec{g}$ until convergence. The initiation and update are shown in equations (2) and (3):

$$Initialization: \quad k = 0, \qquad \vec{g}^0 = \mathbf{H}^T \cdot \vec{f} \tag{2}$$

$$Update: \quad k = k + 1, \quad \vec{g}^{k+1} = \vec{g}^k \cdot \mathbf{H}^T \cdot \left(\frac{\vec{f}}{\mathbf{H} \cdot \vec{g}^k}\right) \tag{3}$$

Where superscript T represents the transpose operator and k denotes the iteration times. In the update section, $\mathbf{H} \cdot \vec{g}^k$ represents the forward projection process from the estimated 3D volume to the estimated 2D light field image. The pixel-wise discrepancies between the estimated 2D light field image and the true raw light field image are calculated with the term $\frac{\vec{f}}{\mathbf{H} \cdot \vec{g}^k}$, where the division denotes the element-wise division operator. The discrepancies are backward projected through $\mathbf{H}^T \cdot \left(\frac{\vec{f}}{\mathbf{H} \cdot \vec{g}^k}\right)$ to update the estimated volume. Since the PSF is shift-invariant within each axial plane, forward and backward projection can be computed with 2D convolution using Fast Fourier Transform (FFT)[6,11]. To speed up the

reconstruction, we implemented Graphics Processing Unit (GPU) acceleration. For all the reconstruction in this work, we set the total number of iterations to be 10. After 10 iterations, discernible differences were generally not observed in the reconstructed volume. Detailed discussion on the time cost of the reconstruction is provided in Supplementary Note 2.

3D temporal difference analysis. The temporal difference analysis is preceded by 3D spatial filtering and voxel-wise temporal filtering. First, each reconstructed 3D volume was filtered spatially by a 3D median filter of size 5 × 5 × 5 voxels. After the spatial filtering, the signal trace of each voxel was filtered by a low-pass Butterworth filter with cutoff frequency at 3 Hz. The temporal difference analysis was then applied to the filtered 3D reconstruction voxel by voxel. Let's denote a voxel intensity value at any time point t = i as v^i. Consider the timelapse that starts at t = 0 and ends at t= T. The temporal difference at t = i of each voxel is defined in (1) as:

$$v_d^i = max(0, v^i - v^{i-1}),\ i \in [2, T) \tag{1}$$

where the negative intensity was set to zero. The temporal difference was computed for all the voxels within the filtered 3D reconstructed region from the second time point to the last time point. The trace of the temporal difference represents the increase in signal intensity at each time point relative to the last time point.

References:

1. Llavador, A., Sola-Pikabea, J., Saavedra, G., Javidi, B. & Martínez-Corral, M. Resolution improvements in integral microscopy with Fourier plane recording. *Optics Express* **24**, 20792 (2016).

2. Scrofani, G. *et al.* FIMic: design for ultimate 3D-integral microscopy of in-vivo biological samples. *Biomed Opt Express* **9**, 335–346 (2017).

3. Galdón, L., Saavedra, G., Garcia-Sucerquia, J., Martínez-Corral, M. & Sánchez-Ortiga, E. Fourier lightfield microscopy: a practical design guide. *Applied Optics* **61**, 2558 (2022).

4. Edelstein, A. D. *et al.* Advanced methods of microscope control using μManager software. *J Biol Methods* **1**, e10 (2014).

5. Zhong, L. *et al.* Essential role of Skp2-mediated p27 degradation in growth and adaptive expansion of pancreatic beta cells. *J Clin Invest* **117**, 2869–2876 (2007).

6. Guo, C., Liu, W., Hua, X., Li, H. & Jia, S. Fourier light-field microscopy. *Opt Express* **27**, 25573–25594 (2019).

7. Broxton, M. *et al.* Wave optics theory and 3-D deconvolution for the light field microscope. *Opt Express* **21**, 25418–25439 (2013).

8. Prevedel, R. *et al.* Simultaneous whole-animal 3D imaging of neuronal activity using light-field microscopy. *Nat Methods* **11**, 727–730 (2014).

9. Lucy, L. B. An iterative technique for the rectification of observed distributions. *The Astronomical Journal* **79**, 745 (1974).

10. Richardson, W. H. Bayesian-Based Iterative Method of Image Restoration*. *Journal of the Optical Society of America* **62**, 55 (1972).

11. Cong, L. *et al.* Rapid whole brain imaging of neural activity in freely behaving larval zebrafish (Danio rerio). *Elife* **6**, e28158 (2017).